PHYSICAL REVIEW B **94**, 075120 (2016)

Ab initio phonon coupling and optical response of hot electrons in plasmonic metals

Ana M. Brown,[1] Ravishankar Sundararaman,[2] Prineha Narang,[1,2,3] William A. Goddard III,[2,4] and Harry A. Atwater[1,2]
[1]*Thomas J. Watson Laboratories of Applied Physics, California Institute of Technology, Pasadena, California 91125, USA*
[2]*Joint Center for Artificial Photosynthesis, California Institute of Technology, Pasadena, California 91125, USA*
[3]*NG NEXT, 1 Space Park Drive, Redondo Beach, California 90278, USA*
[4]*Materials and Process Simulation Center, California Institute of Technology, Pasadena, California 91125, USA*

(Received 1 February 2016; revised manuscript received 26 July 2016; published 11 August 2016)

Ultrafast laser measurements probe the nonequilibrium dynamics of excited electrons in metals with increasing temporal resolution. Electronic structure calculations can provide a detailed microscopic understanding of hot electron dynamics, but a parameter-free description of pump-probe measurements has not yet been possible, despite intensive research, because of the phenomenological treatment of electron-phonon interactions. We present *ab initio* predictions of the electron-temperature dependent heat capacities and electron-phonon coupling coefficients of plasmonic metals. We find substantial differences from free-electron and semiempirical estimates, especially in noble metals above transient electron temperatures of 2000 K, because of the previously neglected strong dependence of electron-phonon matrix elements on electron energy. We also present first-principles calculations of the electron-temperature dependent dielectric response of hot electrons in plasmonic metals, including direct interband and phonon-assisted intraband transitions, facilitating complete theoretical predictions of the time-resolved optical probe signatures in ultrafast laser experiments.

DOI: 10.1103/PhysRevB.94.075120

I. INTRODUCTION

Understanding the energy transfer mechanisms during thermal nonequilibrium between electrons and the lattice is critical for a wide array of applications. Nonequilibrium electron properties on time scales of 10 s–100 s of femtoseconds are most efficiently observed with pulsed laser measurement techniques [1–7]. Laser irradiation of a metal film or nanostructure with an ultrashort laser pulse pushes the electron gas out of equilibrium; describing the evolution of this nonequilibrium distribution has been the subject of intense research for two decades. A majority of investigations so far employ various approximate models, typically based on free-electron models and empirical electron-phonon interactions, to calculate the energy absorption, electron-electron thermalization, and electron-phonon relaxation [8–19]. However, a complete *ab initio* description of the time evolution and optical response of this nonequilibrium electron gas from femtosecond to picosecond time scales has remained elusive, especially because of the empirical treatment of electron-phonon interactions [20].

The initial electron thermalization via electron-electron scattering is qualitatively described within the Landau theory of Fermi liquids [21–24]. The subsequent relaxation of the high temperature electron gas with the lattice is widely described by the two-temperature model (TTM) [1,5–7,17,20], given by coupled differential equations for the electron and lattice temperatures, T_e and T_l,

$$\begin{aligned} C_e(T_e)\frac{dT_e}{dt} &= \nabla\cdot(\kappa_e\nabla T_e) - G(T_e)\times(T_e - T_l) + S(t),\\ C_l(T_l)\frac{dT_l}{dt} &= \nabla\cdot(\kappa_p\nabla T_l) + G(T_e)\times(T_e - T_l). \end{aligned} \tag{1}$$

Here, κ_e and κ_p are the thermal conductivities of the electrons and phonons, $G(T_e)$ is the electron-phonon coupling factor, $C_e(T_e)$ and $C_l(T_l)$ are the electronic and lattice heat capacities, and $S(t)$ is the source term which describes energy deposition by a laser pulse. In nanostructures, the temperatures become homogeneous in space rapidly and the contributions of the thermal conductivities drop out. A vast majority of studies, both theoretical and experimental, treat the remaining material parameters, $G(T_e)$, $C_e(T_e)$, and $C_l(T_l)$, as phenomenological temperature-independent constants [25–32].

Figure 1 schematically shows the time evolution of the electron and lattice temperatures in a plasmonic metal like gold, and the role of the *temperature-dependent* material properties. The electronic density of states and the resultant electronic heat capacity $C_e(T_e)$ determine the peak electron temperature T_e reached after electron-electron thermalization. The electron-phonon matrix elements and the resulting coupling strength $G(T_e)$ determine the rate of energy transfer from the electrons to the lattice, which along with $C_e(T_e)$ determines the rate of relaxation of T_e. Finally, the phonon density of states and the resulting lattice heat capacity $C_l(T_l)$ determine the rise in lattice temperature T_l.

A key challenge in the quantitative application of TTM models is the determination of these *temperature-dependent* material parameters. With pulsed lasers, it is possible to absorb sufficient energy in plasmonic nanostructures to melt the metal once the electrons and lattice have equilibrated [33]. The highest electron temperature, $T_e^{\max}$, accessible in repeatable measurements is therefore limited only by the equilibrated lattice temperature being less than the melting temperature T_m of the metal [34], which yields the condition $\int_{T_m}^{T_e^{\max}} dT_e C_e(T_e) = \int_{T_0}^{T_m} dT_l C_l(T_l)$. Starting at room temperature $T_0 = 300$ K and using our calculations of the electron and lattice heat capacities, $C_e(T_e)$ and $C_l(T_l)$, we find $T_e^{\max} \approx 5700$, 8300, 7500, and 6700 K, respectively, for aluminum, silver, gold, and copper. For gold and copper in particular, these temperatures are sufficient to change the occupations of the d-bands $\sim$2 eV below the Fermi level. Consequently, it is important to derive the temperature dependence of these material parameters from electronic structure calculations rather than free-electron like models [20].

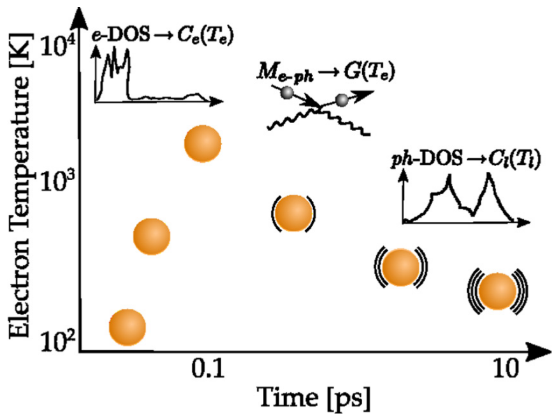

FIG. 1. Schematic electron and lattice temperature evolution with time following laser pulse illumination of a plasmonic metal like gold, along with the relevant material properties that determine this evolution. The vertical position of the gold atoms on the plot corresponds to electron temperature, and the vibration marks around the atoms schematically indicate lattice temperature. We show that both the electron heat-capacity $C_e(T_e)$ [from electronic density of states (DOS)] that sets the peak electron temperature T_e, and the electron-phonon coupling strength $G(T_e)$ (from electron-phonon matrix element $M_{\text{e-ph}}$) that affects the relaxation time of T_e, vary with T_e in a manner sensitive to details of d electrons in noble metals. Only the lattice heat capacity $C_l(T_l)$, that determines the lattice temperature rise, does not vary substantially between the detailed phonon DOS and simpler models.

Therefore to accurately predict the transient optical response of metal nanostructures, we account for the electron-temperature dependence of the electronic heat capacity, electron-phonon coupling factor, and dielectric functions. These properties, in turn, require accurate electron and phonon band structures as well as electron-phonon and optical matrix elements. We recently showed that *ab initio* calculations can quantitatively predict optical response, carrier generation, and electron transport in plasmonic metals in comparison with experiment, with no empirical parameters [35]. In this article, we calculate $C_e(T_e)$, $G(T_e)$ and the temperature and frequency-dependent dielectric function, $\epsilon(\omega,T_e)$, from first principles. These calculations implicitly include electronic-structure effects in the density of states and electron-phonon interaction matrix elements, and implicitly account for processes such as Umklapp scattering. We show substantial differences between our predictions and those from simplified models due to the energy dependence of the electron-phonon matrix elements, especially at high electron temperatures.

The paper is organized as follows. We start with the theoretical background and computational methods used in the calculations of the electron heat capacity, phonon coupling, and temperature dependent dielectric function of plasmonic materials (Sec. II A). In Sec. II B, we show calculations of the electron heat capacity and its dependence on the electron temperature due to the electronic density of states. Analogously, Sec. II C presents the lattice-temperature dependence of the lattice heat capacity due to the phonon density of states. Next, in Sec. II D we show a key result of the paper: temperature dependence of the electron-phonon coupling strength accounting for energy dependence of the electron-phonon matrix elements. Finally, Sec. II E presents the temperature and frequency dependence of the dielectric function, including direct (interband), phonon-assisted, and Drude intraband contributions. Section III summarizes our results and discusses their application to plasmonic nanostructures in various experimental regimes.

II. THEORY AND RESULTS

A. Computational details

We perform density-functional theory (DFT) calculations of the electronic states, phonons, electron-phonon and optical matrix elements, and several derived quantities based on these properties, for four plasmonic metals, aluminum, copper, silver, and gold. We use the open-source plane-wave density-functional software named JDFTx [36] to perform fully relativistic (spinorial) band structure calculations using norm-conserving pseudopotentials at a kinetic energy cutoff of 30 hartrees, and the PBEsol exchange-correlation functional (Perdew-Burke-Ernzerhof functional reparametrized for solids) [37] with a localized $+U$ correction [38] for the d-bands in the noble metals. Reference [39] shows that this method produces accurate electronic band structures in agreement with angle-resolved photoemission (ARPES) measurements within 0.1 eV.

We calculate phonon energies and electron-phonon matrix elements using perturbations on a $4\times4\times4$ supercell. In our calculations, these matrix elements implicitly include Umklapp-like processes. We then convert the electron and phonon Hamiltonians to a maximally localized Wannier function basis [40], with 12^3 k-points in the Brillouin zone for electrons. Specifically, we employ 24 Wannier centers for aluminum and 46 spinorial centers for the noble metals which reproduces the density functional theory (DFT) band structure exactly to at least 50 eV above the Fermi level.

Using this Wannier representation, we interpolate the electron, phonon, and electron-phonon interaction Hamiltonians to arbitrary wave vectors and perform dense Monte Carlo sampling for accurately evaluating the Brillouin zone integrals for each derived property below. This dense Brillouin zone sampling is necessary because of the large disparity in the energy scales of electrons and phonons, and directly calculating DFT phonon properties on dense k-point grids is computationally expensive and impractical. See Ref. [35] for further details on the calculation protocol and benchmarks of the accuracy of the electron-phonon coupling (e.g., resistivity within 5% for all four metals).

B. Electronic density of states and heat capacity

The electronic density of states (DOS) per unit volume

$$g(\varepsilon)=\int_{\text{BZ}}\frac{d\mathbf{k}}{(2\pi)^3}\sum_n\delta(\varepsilon-\varepsilon_{\mathbf{k}n}), \tag{2}$$

where $\varepsilon_{\mathbf{k}n}$ are energies of quasiparticles with band index n and wave vector $\mathbf{k}$ in the Brillouin zone BZ, directly determines the electronic heat capacity and is an important factor in

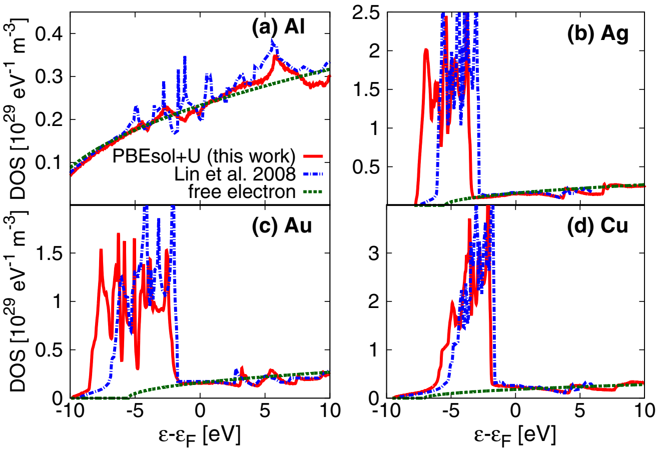

FIG. 2. Comparison of electronic density of states for (a) Al, (b) Ag, (c) Au, and (d) Cu from our relativistic PBEsol+U calculations, previous semilocal PBE DFT calculations [20] (less accurate band structure), and a free electron model.

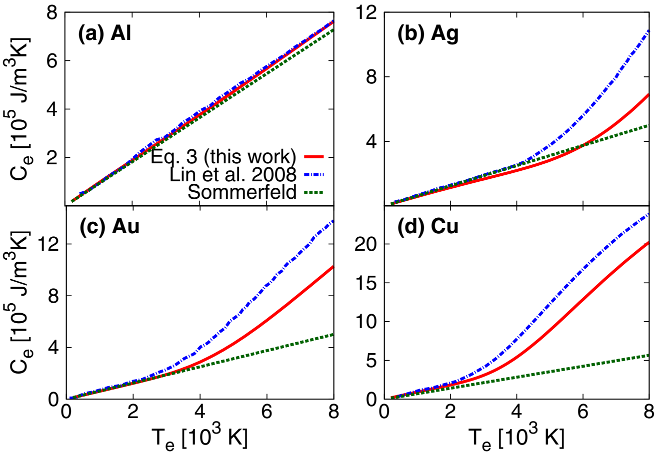

FIG. 3. Comparison of the electronic heat capacity as a function of electron temperature, $C_e(T_e)$, for (a) Al, (b) Ag, (c) Au, and (d) Cu, corresponding to the three electronic density-of-states predictions shown in Fig. 2. The free electron Sommerfeld model underestimates C_e for noble metals at high T_e because it neglects d-band contributions, whereas previous DFT calculations [20] overestimate it because their d-bands are too close to the Fermi level.

the electron-phonon coupling and dielectric response of hot electrons. Above, the band index n implicitly counts spinorial orbitals in our relativistic calculations, and hence we omit the explicit spin degeneracy factor.

Figure 2 compares the DOS predicted by our relativistic PBEsol+U method with a previous nonrelativistic semilocal estimate [20] using the PBE (Perdew-Burke-Ernzerhof) functional [41], as well as a free electron model $\varepsilon_{\mathbf{k}} = \frac{\hbar^2 k^2}{2m_e}$ for which $g(\varepsilon) = \frac{\sqrt{\varepsilon}}{2\pi^2}\left(\frac{2m_e}{\hbar^2}\right)^{3/2}$. The free electron model is a reasonable approximation for aluminum and the PBE and PBEsol+U density-functional calculations also agree reasonably well in this case ($U = 0$ for aluminum). The regular 31^3 k-point grid used for Brillouin zone sampling introduces the sharp artifacts in the DOS from Ref. [20], compared to the much denser Monte Carlo sampling in our calculations with 640 000 k-points for Au, Ag, and Cu, and 1 280 000 k-points for Al.

For the noble metals, the free electron model and the density functional methods agree reasonably near the Fermi level, but differ significantly ∼2 eV below the Fermi level where d-bands contribute. The free electron models ignore the d-bands entirely, whereas the semilocal PBE calculations predict d-bands that are narrower and closer to the Fermi level than the PBEsol+U predictions. The U correction [38] accounts for self-interaction errors in semilocal DFT and positions the d-bands in agreement with ARPES measurements (to within ∼0.1 eV) [39]. Additionally, the DOS in the nonrelativistic PBE calculations strongly peaks at the top of the d-bands (closest to the Fermi level), whereas the DOS in our relativistic calculations is comparatively balanced between the top and middle of the d-bands due to strong spin-orbit splitting, particularly for gold. Below, we find that these inaccuracies in the DOS due to electronic structure methods previously employed for studying hot electrons propagates to the predicted electronic heat capacity and electron-phonon coupling.

The electronic heat capacity, defined as the derivative of the electronic energy per unit volume with respect to the electronic temperature (T_e), can be related to the DOS as

$$C_e(T_e) = \int_{-\infty}^{\infty} d\varepsilon\, g(\varepsilon)\varepsilon \frac{\partial f(\varepsilon,T_e)}{\partial T_e}, \tag{3}$$

where $f(\epsilon,T_e)$ is the Fermi distribution function. The term $\partial f/\partial T_e$ is sharply peaked at the Fermi energy ε_F with a width $\sim k_B T_e$, and therefore the heat capacity depends only on electronic states within a few $k_B T_e$ of the Fermi level. For the free electron model, Taylor expanding $g(\varepsilon)$ around ε_F and analytically integrating (3) yields the Sommerfeld model $C_e(T_e) = \frac{\pi^2 n_e k_B^2}{2\varepsilon_F} T_e$, which is valid for $T_e \ll T_F$ ($\sim 10^5$ K). Above, $n_e = 3\pi^2 k_F^3$, $\varepsilon_F = \frac{\hbar^2 k_F^2}{2m_e}$, and k_F are respectively the number density, Fermi energy, and Fermi wave vector of the free electron model.

At temperatures $T_e \ll T_F$, the electronic heat capacities are much smaller than the lattice heat capacities [5,10,23], which makes it possible for laser pulses to increase T_e by 10^3–10^4 K, while T_l remains relatively constant [6,42,43]. Figure 3 compares $C_e(T_e)$ from the free-electron Sommerfeld model with predictions of (3) using DOS from PBE and PBEsol+U calculations. The free-electron Sommerfeld model is accurate at low temperatures (up to ∼2000 K) for all four metals.

With increasing T_e, $\partial f/\partial T_e$ in (3) is nonzero increasingly further away from the Fermi energy, so that deviations from the free electron DOS eventually become important. For aluminum, the DOS remains free-electron-like over a wide energy range and the Sommerfeld model remains valid throughout. For the noble metals, the increase in DOS due to d-bands causes a dramatic increase in $C_e(T_e)$ once T_e is high enough that $\partial f/\partial T_e$ becomes nonzero in that energy range. Copper and gold have shallower d-bands and deviate at lower temperatures compared to silver. Additionally, the d-bands are too close to the Fermi level in the semilocal PBE calculations of Ref. [20], which results in an overestimation of

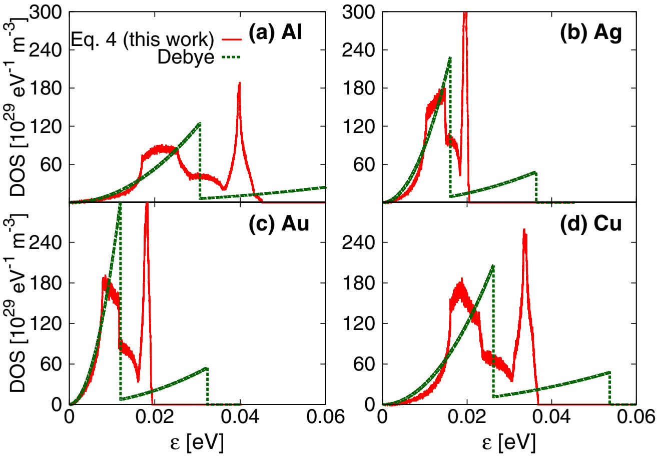

FIG. 4. Comparison of DFT-calculated phonon density of states and the Debye model for (a) Al, (b) Ag, (c) Au, and (d) Cu.

$C_e(T_e)$ compared to our predictions based on the more accurate relativistic PBEsol+U method.

C. Phonon density of states and lattice heat capacity

Similarly, the phonon DOS per unit volume

$$D(\varepsilon) = \int_{\mathrm{BZ}} \frac{d\mathbf{q}}{(2\pi)^3} \sum_{\alpha} \delta(\varepsilon - \hbar\omega_{\mathbf{q}\alpha}), \tag{4}$$

where $\hbar\omega_{\mathbf{q}\alpha}$ are energies of phonons with polarization index α and wave vector $\mathbf{q}$, directly determines the lattice heat capacity,

$$C_l(T_l) = \int_0^\infty d\varepsilon\, D(\varepsilon)\varepsilon \frac{\partial n(\varepsilon, T_l)}{\partial T_l}, \tag{5}$$

where $n(\varepsilon, T_l)$ is the Bose occupation factor.

Within the Debye model, the phonon energies are approximated by an isotropic linear dispersion relation $\omega_{\mathbf{q}\alpha} = v_\alpha q$ up to a maximum Debye wave vector q_D chosen to conserve the number of phonon modes per unit volume. This model yields the analytical phonon DOS, $D(\varepsilon) = \frac{\varepsilon^2}{(2\pi^2)} \sum_\alpha \theta(\hbar q_D v_\alpha - \varepsilon)/(\hbar v_\alpha)^3$, where $v_\alpha = \{v_L, v_T, v_T\}$ are the speeds of sound for the one longitudinal and two degenerate transverse phonon modes of the face-centered cubic metals considered here [34].

Figure 4 compares the DFT-calculated phonon DOS with the Debye model predictions, and shows that the Debye model is a good approximation for the DOS only up to 0.01 eV. However, Fig. 5 shows that the corresponding predictions for the lattice heat capacities are very similar, rapidly approaching the equipartition theorem prediction of $C_l = 3k_B/\Omega$ at high temperatures, which is insensitive to details in the phonon DOS. In fact, the largest deviations of the Debye model are below 100 K and less than 10% from the direct calculations for all four metals. We therefore find that a simple model of the phonons is adequate for predicting the lattice heat capacity, in contrast to the remaining quantities we consider below which are highly sensitive to details of the phonons and their coupling to the electrons.

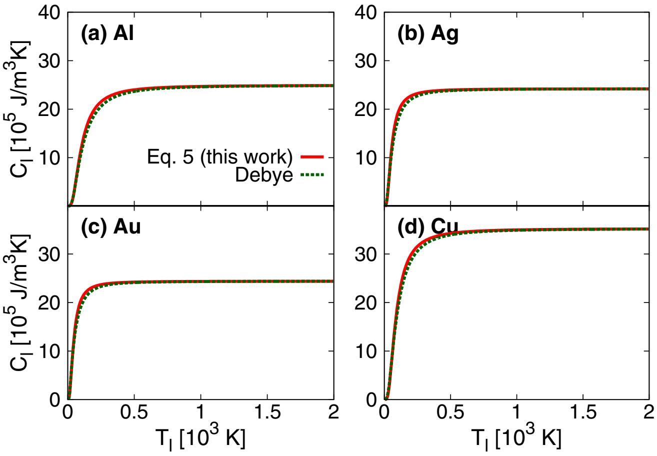

FIG. 5. Comparison of DFT and Debye model predictions of the lattice heat capacity as a function of lattice temperature, $C_l(T_l)$, for (a) Al, (b) Ag, (c) Au, and (d) Cu. Despite large differences in the density of states (Fig. 4), the predicted lattice heat capacities of the two models agree within 10%.

D. Electron-phonon coupling

In Sec. II B we have shown that the electronic heat capacity, which determines the initial temperature that the hot electrons equilibrate to, is sensitive to electronic structure especially in noble metals at high T_e where d-bands contribute. Now we analyze the electron-phonon coupling which determines the subsequent thermalization of the hot electrons with the lattice. We show that details in the electron-phonon matrix elements calculated using DFT also play a significant role, in addition to the electronic band structure, and compare previous semiempirical estimates of the T_e-dependent phonon coupling to our direct calculations.

The rate of energy transfer from electrons at temperature T_e to the lattice (phonons) at temperature T_l per unit volume is given by Fermi's golden rule as

$$\begin{aligned}\frac{dE}{dt} &\equiv G(T_e)(T_e - T_l)\\ &= \frac{2\pi}{\hbar}\int_{\mathrm{BZ}} \frac{\Omega\, d\mathbf{k}\, d\mathbf{k}'}{(2\pi)^6} \sum_{nn'\alpha} \delta(b - \hbar\omega_{\mathbf{k}'-\mathbf{k},\alpha})\\ &\quad \times \hbar\omega_{\mathbf{k}'-\mathbf{k},\alpha} \left|g^{\mathbf{k}'-\mathbf{k},\alpha}_{\mathbf{k}'n',\mathbf{k}n}\right|^2 S_{T_e,T_l}(\varepsilon_{\mathbf{k}n}, \varepsilon_{\mathbf{k}'n'}, \hbar\omega_{\mathbf{k}'-\mathbf{k},\alpha}),\end{aligned} \tag{6}$$

with

$$\begin{aligned}S_{T_e,T_l}(\varepsilon, \varepsilon', \hbar\omega_{\mathrm{ph}}) \equiv{}& f(\varepsilon, T_e) n(\hbar\omega_{\mathrm{ph}}, T_l)(1 - f(\varepsilon', T_e))\\ &- (1 - f(\varepsilon, T_e))(1 + n(\hbar\omega_{\mathrm{ph}}, T_l)) f(\varepsilon', T_e).\end{aligned} \tag{7}$$

Here, Ω is the unit cell volume, $\hbar\omega_{\mathbf{q}\alpha}$ is the energy of a phonon with wave vector $\mathbf{q} = \mathbf{k}' - \mathbf{k}$ and polarization index α, and $g^{\mathbf{k}'-\mathbf{k},\alpha}_{\mathbf{k}'n',\mathbf{k}n}$ is the electron-phonon matrix element coupling this phonon to electronic states indexed by $\mathbf{k}n$ and $\mathbf{k}'n'$.

Above, S is the difference between the product of occupation factors for the forward and reverse directions of the electron-phonon scattering process $\mathbf{k}n + \mathbf{q}\alpha \rightarrow \mathbf{k}'n'$, with $f(\varepsilon, T_e)$ and $n(\hbar\omega, T_l)$ being the Fermi and Bose distribution function for the electrons and phonons, respectively. Using the fact that $S_{T_e,T_e} = 0$ for an energy-conserving process $\varepsilon + \hbar\omega_{\rm ph} = \varepsilon'$ by detailed balance, we can write the electron-phonon coupling coefficient as

$$G(T_e) = \frac{2\pi}{\hbar} \int_{\rm BZ} \frac{\Omega\, d\mathbf{k}\, d\mathbf{k}'}{(2\pi)^6} \sum_{nn'\alpha} \delta(\varepsilon_{\mathbf{k}'n'} - \varepsilon_{\mathbf{k}n} - \hbar\omega_{\mathbf{k}'-\mathbf{k},\alpha}) \\ \times \hbar\omega_{\mathbf{k}'-\mathbf{k},\alpha} \left| g^{\mathbf{k}'-\mathbf{k},\alpha}_{\mathbf{k}'n',\mathbf{k}n} \right|^2 (f(\varepsilon_{\mathbf{k}n},T_e) - f(\varepsilon_{\mathbf{k}'n'},T_e)) \\ \times \frac{n(\hbar\omega_{\mathbf{k}'-\mathbf{k},\alpha},T_e) - n(\hbar\omega_{\mathbf{k}'-\mathbf{k},\alpha},T_l)}{T_e - T_l}. \qquad (8)$$

This general form for *DFT-based* electronic and phononic states is analogous to previous single-band/free electron theories of the electron-phonon coupling coefficient; see, for example, the derivation by Allen *et al.* [44]. Note that unlike previous empirical models, here the coupling coefficient depends on the lattice temperature T_l as well, but we omit the T_l label in $G(T_e)$ to keep the notation consistent with previous approaches [20], and present results below for $T_l = 298$ K (ambient temperature).

The direct evaluation of $G(T_e)$ using (8) requires a six-dimensional integral over electron-phonon matrix elements from DFT with very fine k-point grids that can resolve both electronic and phononic energy scales. This is impractical without the recently developed Wannier interpolation and Monte Carlo sampling methods for these matrix elements [35,45], and therefore our results are the first parameter-free predictions of $G(T_e)$, derived entirely from DFT.

Previous theoretical estimates of $G(T_e)$ are semiempirical, combining DFT electronic structure with empirical models for the phonon coupling. For example, Wang *et al.* [46] assume that the electron-phonon matrix elements averaged over scattering angles is independent of energy and that the phonon energies are smaller than k_BT_e, and then approximate the electron-phonon coupling coefficient as

$$G(T_e) \approx \frac{\pi k_B}{\hbar g(\varepsilon_F)} \lambda\langle(\hbar\omega)^2\rangle \int_{-\infty}^{\infty} d\varepsilon\, g^2(\varepsilon) \frac{-\partial f(\varepsilon,T_e)}{\partial\varepsilon}, \qquad (9)$$

where λ is the electron-phonon mass enhancement parameter and $\langle(\hbar\omega)^2\rangle$ is the second moment of the phonon spectrum [8,20,47]. Lin *et al.* [20] treat $\lambda\langle(\hbar\omega)^2\rangle$ as an empirical parameter calibrated to experimental $G(T_e)$ at low T_e obtained from thermoreflectance measurements, and extrapolate it to higher T_e using (9). See Refs. [46] and [20] for more details.

For clarity, we motivate here a simpler derivation of an expression of the form of (9) from the general form (8). First, making the approximation $\hbar\omega_{\mathbf{q}\alpha} \ll T_e$ (which is reasonably valid for T_e above room temperature) allows us to approximate the difference between the electron occupation factors in the second line of (8) by $\hbar\omega_{\mathbf{q}\alpha}\partial f/\partial\varepsilon$ (using energy conservation). Additionally, for $T_e \gg T_l$, the third line of (8) simplifies to $k_B/(\hbar\omega_{\mathbf{k}'-\mathbf{k},\alpha})$. With no other approximations, we can then rearrange (8) to collect contributions by initial electron energy,

$$G(T_e) \approx \frac{\pi k_B}{\hbar g(\varepsilon_F)} \int_{-\infty}^{\infty} d\varepsilon\, h(\varepsilon) g^2(\varepsilon) \frac{-\partial f(\varepsilon,T_e)}{\partial\varepsilon}, \qquad (10)$$

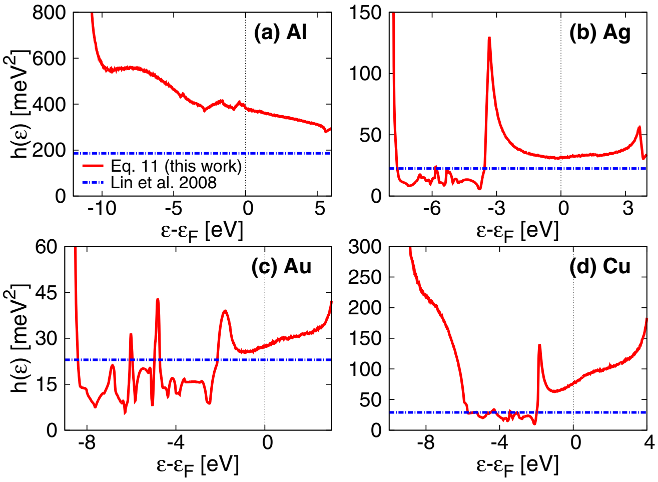

FIG. 6. Energy-resolved electron-phonon coupling strength $h(\varepsilon)$, defined by (11), for (a) Al, (b) Ag, (c) Au, and (d) Cu. For the noble metals, $h(\epsilon_F)$ is substantially larger than its value in the d-bands, which causes previous semiempirical estimates [20] using a constant $h(\varepsilon)$ to overestimate the electron-phonon coupling [$G(T_e)$] at $T_e \gtrsim 3000$ K, as shown in Fig. 7.

with

$$h(\varepsilon) \equiv \frac{2g(\varepsilon_F)}{g^2(\varepsilon)} \int_{\rm BZ} \frac{\Omega\, d\mathbf{k}\, d\mathbf{k}'}{(2\pi)^6} \sum_{nn'\alpha} \delta(\varepsilon - \varepsilon_{\mathbf{k}n}) \\ \times \delta(\varepsilon_{\mathbf{k}'n'} - \varepsilon_{\mathbf{k}n} - \hbar\omega_{\mathbf{k}'-\mathbf{k},\alpha}) \hbar\omega_{\mathbf{k}'-\mathbf{k},\alpha} \left| g^{\mathbf{k}'-\mathbf{k},\alpha}_{\mathbf{k}'n',\mathbf{k}n} \right|^2. \qquad (11)$$

Therefore, the primary approximation in previous semiempirical estimates [20,46] is the replacement of $h(\varepsilon)$ by an energy-independent constant $\lambda\langle(\hbar\omega)^2\rangle$, used as an empirical parameter.

Figure 6 compares our calculations of this energy-resolved electron-phonon coupling strength, $h(\varepsilon)$, with previous empirical estimates of $\lambda\langle(\hbar\omega)^2\rangle$, and Fig. 7 compares the resulting temperature dependence of the electron-phonon coupling, $G(T_e)$, from (8) and semiempirical methods (9). For noble metals, $G(T_e)$ increases sharply beyond $T_e \sim 3000$ K because of the large density of states in the d-bands. However, $h(\varepsilon)$ is smaller by a factor of 2–3 in the d-bands compared to near the Fermi level. Therefore, assuming $h(\varepsilon)$ to be an empirical constant [17,20] results in a significant overestimate of $G(T_e)$ at high T_e, compared to the direct calculations. Additionally, the shallowness of the d-bands in the semilocal PBE band structure used in Ref. [20] lowers the onset temperature of the increase in $G(T_e)$, and results in further overestimation compared to our predictions.

Our predictions agree very well with the experimental measurements of $G(T_e)$ available at lower temperatures for noble metals [3,14,15,32,48]. In fact, the semiempirical calculation based on $\lambda\langle(\hbar\omega)^2\rangle$ underestimates the room temperature electron-phonon coupling for these metals; the significant overestimation of $G(T_e)$ seen in Fig. 7 is despite this partial cancellation of error. This shows the importance of detailed DFT electron-phonon matrix elements in calculating the coupling between hot electrons and the lattice.

Experimental measurements of the electron-phonon coupling in noble metals are reliable because of the reasonably

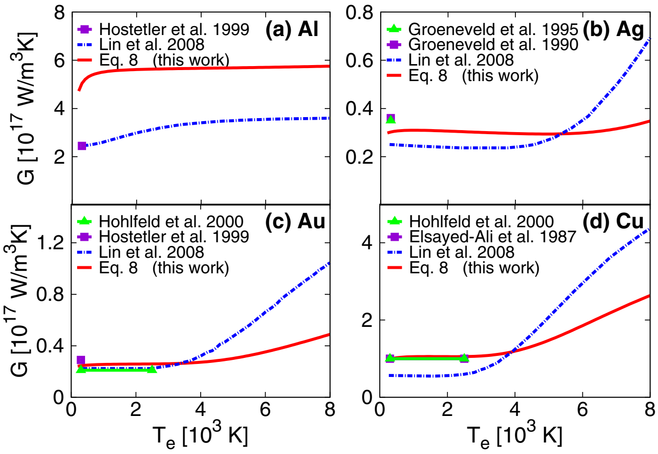

FIG. 7. Comparison of predictions of the electron-phonon coupling strength as a function of electron temperature, $G(T_e)$, for (a) Al, (b) Ag, (c) Au, and (d) Cu, with experimental measurements where available [3,14,15,32,48]. The DFT-based semiempirical predictions of Lin *et al.* [20] overestimate the coupling for noble metals at high temperatures because they assume an energy-independent electron-phonon coupling strength (Fig. 6) and neglect the weaker phonon coupling of d-bands compared to the conduction band. The experimental results (and hence the semiempirical predictions) for aluminum underestimate electron-phonon coupling because they include the effect of competing electron-electron thermalization which happens on the same time scale.

clear separation between a fast electron-electron thermalization rise followed by a slower electron-phonon decay in the thermoreflectance signal. In aluminum, these time scales significantly overlap resulting in strong nonequilibrium effects and making experimental determination of the equilibrium electron-phonon coupling $G(T_e)$ difficult. Consequently, the value of $G(T_e)$ for Al is not well agreed upon [32,49]. Using a simplified single-band free-electron-like model of the electrons, Ref. [50] estimates $G \approx 2.9 \times 10^7$ W/m^{3}K for thermalized electrons at 2000 K, which is 1.5× larger than $G \approx 1.9 \times 10^7$ W/m^{3}K for nonthermalized electrons with the same amount of energy. In Fig. 7(a), our predictions using (8) which assumes equilibrium are 2× larger than the experimental estimates [32] which implicitly include the nonequilibrium effects. On the other hand, the semiempirical model of Ref. [20] assumes thermalized electrons, but fits to experimental data that includes nonthermal effects (and matches experiment by construction). The single-band-model nonequilibrium predictions do not match experiment because it assumes a simple model for electron-phonon matrix elements that ignores Umklapp processes [50]. Ultimately, quantitative agreement with experiments for aluminum (for the right reasons) therefore requires an extension of our nonempirical DFT approach (8) to include nonequilibrium effects, a subject of current work in our group.

E. Dielectric function

The final ingredient for a complete theoretical description of ultrafast transient absorption measurements is the temperature-dependent dielectric function of the material. We previously showed [35] that we could predict the imaginary part of the dielectric function $\mathrm{Im}\,\epsilon(\omega)$ of plasmonic metals in quantitative agreement with ellipsometric measurements for a wide range of frequencies by accounting for the three dominant contributions,

$$\mathrm{Im}\,\epsilon(\omega) = \frac{4\pi\sigma_0}{\omega(1+\omega^2\tau^2)} + \mathrm{Im}\,\epsilon_{\mathrm{direct}}(\omega) + \mathrm{Im}\,\epsilon_{\mathrm{phonon}}(\omega). \tag{12}$$

We briefly summarize the calculation of these contributions and focus on their electron temperature dependence below; see Ref. [35] for a detailed description.

The first term of (12) accounts for the Drude response of the metal due to free carriers near the Fermi level, with the zero-frequency conductivity σ_0 and momentum relaxation time τ calculated using the linearized Boltzmann equation with collision integrals based on DFT [35]. The second and third terms of (12),

$$\mathrm{Im}\,\epsilon_{\mathrm{direct}}(\omega) = \frac{4\pi^2 e^2}{m_e^2\omega^2}\int_{\mathrm{BZ}}\frac{d\mathbf{k}}{(2\pi)^3}\sum_{n'n}(f_{\mathbf{k}n} - f_{\mathbf{k}n'})\delta(\varepsilon_{\mathbf{k}n'} - \varepsilon_{\mathbf{k}n} - \hbar\omega)\left|\hat{\boldsymbol{\lambda}}\cdot\langle\mathbf{p}\rangle^{\mathbf{k}}_{n'n}\right|^2, \tag{13}$$

$$\begin{aligned}\mathrm{Im}\,\epsilon_{\mathrm{phonon}}(\omega) = {}& \frac{4\pi^2 e^2}{m_e^2\omega^2}\int_{\mathrm{BZ}}\frac{d\mathbf{k}'d\mathbf{k}}{(2\pi)^6}\sum_{n'n\alpha\pm}(f_{\mathbf{k}n} - f_{\mathbf{k}'n'})\left(n_{\mathbf{k}'-\mathbf{k},\alpha} + \frac{1}{2} \mp \frac{1}{2}\right)\delta(\varepsilon_{\mathbf{k}'n'} - \varepsilon_{\mathbf{k}n} - \hbar\omega \mp \hbar\omega_{\mathbf{k}'-\mathbf{k},\alpha})\\ &\times\left|\hat{\boldsymbol{\lambda}}\cdot\sum_{n_1}\left(\frac{g^{\mathbf{k}'-\mathbf{k},\alpha}_{\mathbf{k}'n',\mathbf{k}n_1}\langle\mathbf{p}\rangle^{\mathbf{k}}_{n_1 n}}{\varepsilon_{\mathbf{k}n_1} - \varepsilon_{\mathbf{k}n} - \hbar\omega + i\eta} + \frac{\langle\mathbf{p}\rangle^{\mathbf{k}'}_{n'n_1} g^{\mathbf{k}'-\mathbf{k},\alpha}_{\mathbf{k}'n_1,\mathbf{k}n}}{\varepsilon_{\mathbf{k}'n_1} - \varepsilon_{\mathbf{k}n} \mp \hbar\omega_{\mathbf{k}'-\mathbf{k},\alpha} + i\eta}\right)\right|^2,\end{aligned} \tag{14}$$

capture the contributions due to direct interband excitations and phonon-assisted intraband excitations, respectively. Here $\langle\mathbf{p}\rangle^{\mathbf{k}}_{n'n}$ are matrix elements of the momentum operator, $\hat{\boldsymbol{\lambda}}$ is the electric field direction (results are isotropic for crystals with cubic symmetry), and all remaining electron and phonon properties are exactly as described previously. The energy-conserving δ functions are replaced by a Lorentzian of width equal to the sum of initial and final electron linewidths, because of the finite lifetime of the quasiparticles.

The dielectric function calculated using (12)–(14) depends on the electron temperature T_e in two ways. First, the electron occupations $f_{\mathbf{k}n}$ directly depend on T_e. Second, the phase space for electron-electron scattering increases with electron temperature, which increases the Lorentzian broadening in the energy conserving δ functions in (13) and (14).

TABLE I. Coefficient of the temperature dependence of the electron-electron scattering rate as given by (15), extracted from fits to the energy dependence of DFT-calculated electron-electron scattering rates at room temperature [35].

Metal	Al	Ag	Au	Cu
D_e (eV^{-1})	0.017	0.021	0.016	0.020

We calculate electron linewidths from DFT using Fermi golden rule calculations for electron-electron and electron-phonon scattering at room temperature, as detailed in Ref. [35]. These calculations are computationally expensive and difficult to repeat for several electron temperatures; we instead use the linewidths at room temperature with an analytical correction for the T_e dependence. The electron-phonon scattering rate depends on the lattice temperature, but is approximately independent of T_e because the phase space for scattering is determined primarily by the electronic density of states and electron-phonon matrix elements, which depend strongly on the electron energies but not on the occupation factors or T_e. The phase space for electron-electron scattering, on the other hand, depends on the occupation factors and T_e because an electron at an energy far from the Fermi level can scatter with electrons close to the Fermi level. The variation of this phase space with temperature is primarily due to the change in occupation of states near the Fermi level, and we can therefore estimate this effect in plasmonic metals using a free electron model.

Within a free electron model, the phase space for electron-electron scattering grows quadratically with energy relative to the Fermi level, resulting in scattering rates $\propto(\varepsilon-\varepsilon_F)^2$ at zero electron temperatures, as is well known [2,51]. We can extend these derivations to finite electron temperature to show that the energy and temperature-dependent electron-electron scattering rate

$$\tau_{\mathrm{ee}}^{-1}(\varepsilon,T_e) \approx \frac{D_e}{\hbar}[(\varepsilon-\varepsilon_F)^2+(\pi k_B T_e)^2] \qquad (15)$$

for $|\varepsilon-\varepsilon_F| \ll \varepsilon_F$ and $T_e \ll \varepsilon_F/k_B$. Within the free electron model, the constant of proportionality $D_e = \frac{m_e e^4}{4\pi\hbar^2(\epsilon_b^0)^2\varepsilon_S^{3/2}\sqrt{\varepsilon_F}}\left(\frac{\sqrt{4\varepsilon_F\varepsilon_S}}{4\varepsilon_F+\varepsilon_S}+\tan^{-1}\sqrt{\frac{4\varepsilon_F}{\varepsilon_S}}\right)$, where the background dielectric constant ϵ_b^0 and the Thomas-Fermi screening energy scale ε_S are typically treated as empirical parameters [2]. Here, we extract D_e by fitting (15) to the electron-electron scattering rates at room temperature T_0 calculated using DFT [35]. The resulting fit parameters are listed in Table I. We then estimate the total scattering rates at other temperatures by adding $(D_e/\hbar)(\pi k_B)^2(T_e^2-T_0^2)$ to the total DFT-calculated results (including electron-phonon scattering) at T_0. Note that we could have equivalently fit the DFT-calculated scattering rates at zero temperature, but the Fermi golden rule results at room temperature are less noisy at finite k-point sampling, and moreover these rates do not differ appreciably for electron energies more than $\sim\pi k_B T_0 \approx 0.08$ eV away from the Fermi level anyway.

Finally, we use the Kramers-Kronig relations to calculate $\mathrm{Re}(\epsilon(\omega,T_e))$ from $\mathrm{Im}(\epsilon(\omega,T_e))$. Figure 8 compares the DFT-predicted dielectric functions with ellipsometry measurements [52] for a range of frequencies spanning from near-infrared to ultraviolet. Note that we scale the y axis by $(\omega/\omega_p)^2$, where $\omega_p=\sqrt{4\pi e^2 n_e/m_e}$ is the free-electron plasma frequency, in order to display features at all frequencies on the same scale. We find excellent agreement for aluminum within 10% of experiment over the entire frequency range, including the peak around 1.6 eV due to an interband transition. The agreement is reasonable for noble metals with a typical error within 20%, but with a larger error ∼50% for certain features in the interband $d \rightarrow s$ transitions due to inaccuracies in the d-band positions predicted by DFT (especially for silver). In the present work, the PBEsol+U band structure is typically accurate to ∼0.1 eV [39], compared to errors ∼1 eV in d-band positions predicted by semilocal DFT functionals [20] and qualitative inadequacies of free-electron-like models that ignore d bands entirely. Consequently, our chosen method has the potential to provide the most reliable predictions of metal dielectric functions, especially for the electron temperature dependence that we discuss next. (Empirical fits such as Drude-Lorentz models can be more accurate by construction at one temperature [53], but do not predict temperature dependence.)

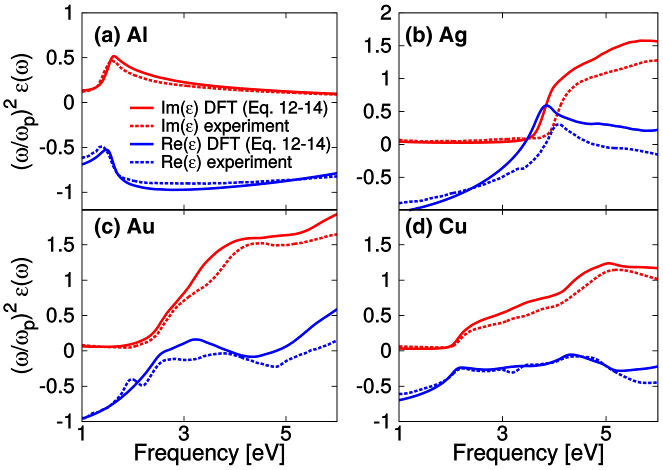

FIG. 8. DFT predictions of the complex dielectric functions for (a) Al, (b) Ag, (c) Au, and (d) Cu at room temperature (300 K) compared with ellipsometry measurements [52]. The y axis is scaled by ω^2/ω_p^2 in order to represent features at different frequencies such as the Drude pole and the interband response on the same scale.

Figures 9–11 show the change of the DFT-calculated complex dielectric function (solid lines) upon increasing the electron temperature T_e from room temperature to 400 K, 1000 K, and 5000 K, respectively, while the lattice remains at room temperature (see Supplemental Material [54]). For all four metals, the response from infrared to ultraviolet frequencies is dominated by "sharp" features due to interband transitions that broaden with increasing temperature. In the remainder of this section, we analyze these sharp interband features in greater detail using a simpler analytic model of the ($d \rightarrow s$) transitions (shown in dashed lines in the aforementioned figures).

The strongest temperature dependence in noble metals results from transitions between the highest occupied d-band to the Fermi level near the L point, as shown in Fig. 12(a). Assuming a parabolic dispersion and a constant transition

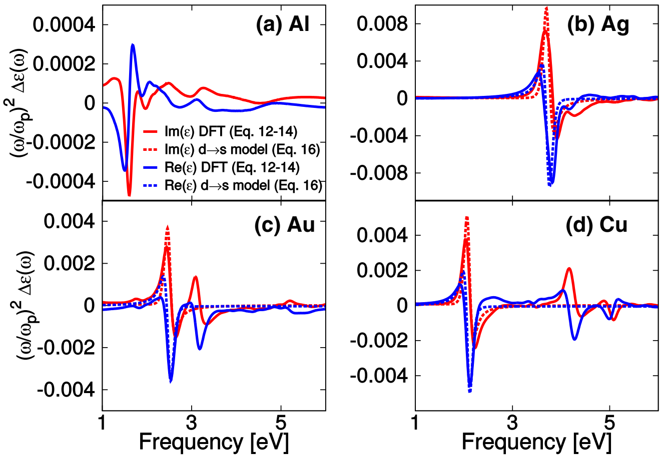

FIG. 9. Change in the DFT-predicted complex dielectric function (solid lines) for (a) Al, (b) Ag, (c) Au, and (d) Cu from room temperature (300 K) to electron temperature $T_e = 400$ K (with the lattice remaining at room temperature). In comparison, the analytical $d \to s$ model (16) (dashed lines) captures essential features of the DFT results for noble metals at lower temperatures, but misses the contributions of broadening due to electron-electron scattering at higher temperatures. Note that the y axis is scaled as in Fig. 8 for clarity.

matrix element, this temperature dependence can be modeled as [17,55]

$$\Delta\epsilon(\omega) = -\Delta\mathcal{K}\frac{A_0}{(\hbar\omega)^2}\int_{-\varepsilon_c}^{\infty}\frac{d\varepsilon(1-f(\varepsilon,T_e))}{\sqrt{(m_v^*/m_c^*)(\hbar\omega-(\varepsilon+\varepsilon_0+\varepsilon_c)) -(\varepsilon+\varepsilon_c)}}. \tag{16}$$

The denominator captures the joint density of states for transitions between the bands, and the numerator counts unoccupied states near the Fermi level, which introduces the temperature dependence. Above, $\mathcal{K}$ fills in the real part of the dielectric function, given the imaginary part using the Kramers-Kronig relation.

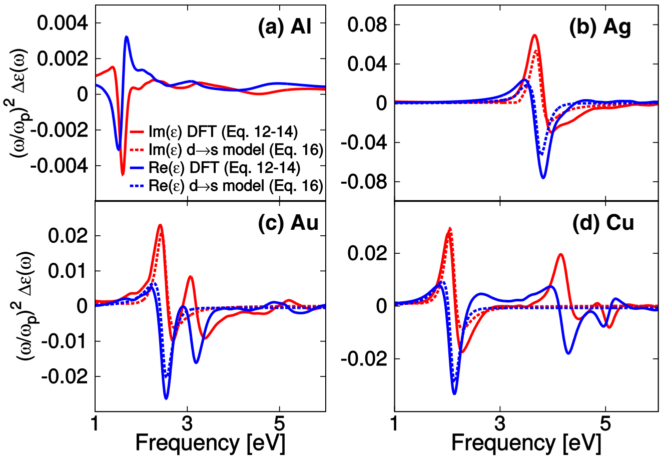

FIG. 10. Change in the DFT-predicted complex dielectric function (solid lines) for (a) Al, (b) Ag, (c) Au, and (d) Cu from room temperature (300 K) to electron temperature $T_e = 1000$ K (with the lattice remaining at room temperature), compared to the analytical $d \to s$ model (16) (dashed lines).

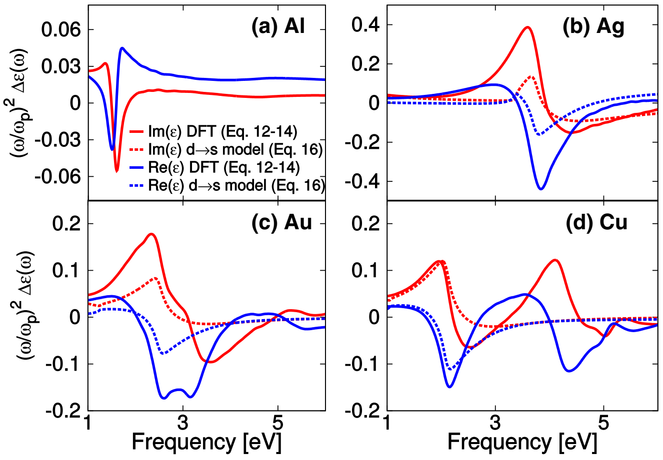

FIG. 11. Change in the DFT-predicted complex dielectric function (solid lines) for (a) Al, (b) Ag, (c) Au, and (d) Cu from room temperature (300 K) to electron temperature $T_e = 5000$ K (with the lattice remaining at room temperature), compared to the analytical $d \to s$ model (16) (dashed lines).

Table II lists the parameters for the parabolic band approximation obtained from the PBEsol+U band structures. Figure 9 shows that this approximation (dashed lines) captures the correct shape of $\Delta\varepsilon(\omega)$ for small changes in T_e. However, this model underestimates the T_e dependence for higher T_e because it ignores the quadratic increase in broadening of the electronic states due to increased electron-electron scattering, as Figs. 10 and 11 show. Aluminum exhibits a sharp change in the dielectric function around $\hbar\omega \approx 1.5$ eV, which results from several transitions to/from the Fermi level near the W point as Fig. 12(b) shows. Additionally two of the involved bands are not parabolic, making it difficult to construct a simple model like (16). Therefore, simplified models are adequate for qualitative analysis of lower temperature excitation experiments in noble metals [17], but dielectric functions from first-principles DFT calculations are necessary for a quantitative analysis of higher temperature experiments and a wider range of materials and probe frequencies.

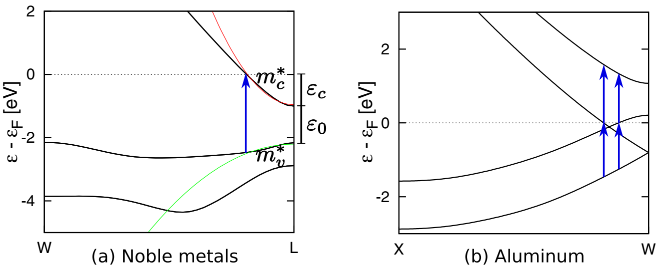

FIG. 12. Critical interband transitions determining the “sharp” features in the dielectric function change for (a) noble metals (gold shown; similar shapes for silver and copper) and (b) aluminum. A parabolic band model around the L point (parameters in Table II) approximates the critical transition in noble metals. This is difficult in aluminum because of four such transitions in a narrow energy range ≈1.3–1.6 eV.

TABLE II. Parameters to describe the change in dielectric function of noble metals with electron temperature using the $d \to s$ model (16) with a parabolic band approximation, extracted from fits to the PBEsol+U band structure. The energies and effective masses are also labeled in Fig. 12(a).

	Ag	Au	Cu
Physical constants:			
ω_p (eV/$\hbar$)	8.98	9.01	10.8
τ^{-1} (eV/$\hbar$)	0.0175	0.0240	0.0268
Fits to DFT calculations:			
A_0 (eV$^{3/2}$)	70	22	90
ε_c (eV)	0.31	0.96	0.98
ε_0 (eV)	3.36	1.25	1.05
m_v^*/m_c^*	5.4	3.4	16.1

III. CONCLUSIONS

Our parameter-free DFT calculations of electron-phonon coupling, electron, and lattice heat capacities, and dielectric functions show qualitative differences from free-electron and previous semiempirical estimates because of the substantial energy dependence of electron-phonon matrix elements and electronic density of states. These changes are particularly important for gold and copper at transient electron temperatures greater than 2000 K because of the change in occupations of the d-bands situated ~2 eV below the Fermi level in these metals.

The temperature dependence of the optical response is, in particular, important for a wide range of applications beyond understanding ultrafast measurements. We show that while simple models can account for some of the qualitative features of the change in dielectric function for small changes in temperature, an electronic structure treatment is essential to quantitatively account for the complete frequency and temperature dependence, including effects such as carrier linewidth broadening and transitions between multiple nonparabolic bands. Given the dearth of published temperature-dependent dielectric functions in the literature, we include detailed tables of our predictions for electron temperatures up to 8000 K, and spanning frequencies from the infrared to the ultraviolet, in the Supplemental Material [54].

This work has direct implications for analysis of experimental pump-probe studies of metal nanostructures and is the subject of ongoing work in our group. With the predicted material properties we anticipate a parameter-free description of the spectra obtained in transient absorption studies since we implicitly account for all the microscopic processes in the nonequilibrium dynamics of electrons in plasmonic metals.

ACKNOWLEDGMENTS

This material is based upon work performed by the Joint Center for Artificial Photosynthesis, a DOE Energy Innovation Hub, supported through the Office of Science of the U.S. Department of Energy under Award No. DE-SC0004993. This research used resources of the National Energy Research Scientific Computing Center, a DOE Office of Science User Facility supported by the Office of Science of the U.S. Department of Energy under Contract No. DE-AC02-05CH11231. P.N. and W.A.G. acknowledge financial support from NG NEXT for this project. P.N. is supported by a National Science Foundation Graduate Research Fellowship and by the Resnick Sustainability Institute. A.B. is supported by a National Science Foundation Graduate Research Fellowship, a Link Foundation Energy Fellowship, and the DOE "Light-Material Interactions in Energy Conversion" Energy Frontier Research Center (Grant No. DE-SC0001293).

[1] S. I. Anisimov, B. L. Kapeliovich, and T. L. Perel'man, Zh. Eksp. Teor. Fiz. **66**, 776 (1974) [J. Exp. Theor. Phys. **39**, 375 (1974)].
[2] N. Del Fatti, C. Voisin, M. Achermann, S. Tzortzakis, D. Christofilos, and F. Vallée, Phys. Rev. B **61**, 16956 (2000).
[3] H. Elsayed-Ali, T. Norris, M. Pessot, and G. Mourou, Phys. Rev. Lett. **58**, 1212 (1987).
[4] H. E. Elsayed-Ali, T. Juhasz, G. O. Smith, and W. E. Bron, Phys. Rev. B **43**, 4488 (1991).
[5] A. Giri, J. T. Gaskins, B. M. Foley, R. Cheaito, and P. E. Hopkins, J. Appl. Phys. **117**, 044305 (2015).
[6] G. V. Hartland, Chem. Rev. **111**, 3858 (2011).
[7] M. I. Kaganov, I. M. Lifshitz, and L. V. Tanatarov, Zh. Eksp. Teor. Fiz. **31**, 232 (1957) [J. Exp. Theor. Phys. **4**, 173 (1957)].
[8] G. Grimvall, *The Electron-phonon Interaction in Metals* (North-Holland, New York, 1981), Vol. 8.
[9] Y. Gan, C. Wang, and Z. Chen, Opt. Lett. **40**, 340 (2015).
[10] S. Link and M. A. El-Sayed, J. Phys. Chem. B **103**, 8410 (1999).
[11] T. Luo and G. Chen, Phys. Chem. Chem. Phys. **15**, 3389 (2013).
[12] P. M. Norris, A. P. Caffrey, R. J. Stevens, J. M. Klopf, J. T. McLeskey, and A. N. Smith, Rev. Sci. Instrum. **74**, 400 (2003).
[13] B. Y. Mueller and B. Rethfeld, Appl. Surf. Sci. **302**, 24 (2014).
[14] R. H. Groeneveld, R. Sprik, and A. Lagendijk, Phys. Rev. Lett. **64**, 784 (1990).
[15] R. H. Groeneveld, R. Sprik, and A. Lagendijk, Phys. Rev. B **51**, 11433 (1995).
[16] B. Rethfeld, A. Kaiser, M. Vicanek, and G. Simon, Phys. Rev. B **65**, 214303 (2002).
[17] C.-K. Sun, F. Vallée, L. H. Acioli, E. P. Ippen, and J. G. Fujimoto, Phys. Rev. B **50**, 15337 (1994).
[18] Y. Ma, J. Appl. Phys. **116**, 243505 (2014).
[19] A. J. Leenheer, P. Narang, N. S. Lewis, and H. A. Atwater, J. Appl. Phys. **115**, 134301 (2014).
[20] Z. Lin and L. V. Zhigilei, Phys. Rev. B **77**, 075133 (2008).
[21] L. D. Landau and E. M. Lifschitz, *Electrodynamics of Continuous Media, Course of Theoretical Physics* (Pergamon Press, Oxford, 1960), Vol. 8.
[22] J. M. Ziman, *Electrons and Phonons* (Clarendon Press, Oxford, 1962).
[23] N. W. Ashcroft and N. D. Mermin, *Solid State Physics* (Holt, Rinehart and Winston, New York, 1976).
[24] D. Pines and P. Nozieres, *Normal Fermi Liquids, The Theory of Quantum Liquids* (Addison-Wesley, New York, 1966), Vol. 1.
[25] H. Inouye, K. Tanaka, I. Tanahashi, and K. Hirao, Phys. Rev. B **57**, 11334 (1998).

[26] E. Knoesel, A. Hotzel, and M. Wolf, Phys. Rev. B **57**, 12812 (1998).
[27] J. Gavnholt, A. Rubio, T. Olsen, K. Thygesen, and J. Schiotz, Phys. Rev. B **79**, 195405 (2009).
[28] E. Carpene, Phys. Rev. B **74**, 024301 (2006).
[29] S. Brorson, J. Fujimoto, and E. Ippen, Phys. Rev. Lett. **59**, 1962 (1987).
[30] C. Frischkorn and M. Wolf, Chem. Rev. **106**, 4207 (2006).
[31] H. Harutyunyan, A. B. F. Martinson, D. Rosenmann, L. K. Khorashad, L. V. Besteiro, A. O. Govorov, and G. P. Wiederrecht, Nat. Nanotechnol. **10**, 770 (2015).
[32] J. L. Hostetler, A. N. Smith, D. M. Czajkowsky, and P. M. Norris, Appl. Opt. **38**, 3614 (1999).
[33] S. Link, C. Burda, M. B. Mohamed, B. Nikoobakht, and M. A. El-Sayed, J. Phys. Chem. A **103**, 1165 (1999).
[34] D. Lide, *CRC Handbook of Chemistry and Physics, 84th ed.* (Taylor & Francis, London, 2003).
[35] A. Brown, R. Sundararaman, P. Narang, W. A. Goddard III, and H. A. Atwater, ACS Nano **10**, 957 (2016).
[36] R. Sundararaman, D. Gunceler, K. Letchworth-Weaver, and T. A. Arias, JDFTx, http://jdftx.sourceforge.net.
[37] J. P. Perdew, A. Ruzsinszky, G. I. Csonka, O. A. Vydrov, G. E. Scuseria, L. A. Constantin, X. Zhou, and K. Burke, Phys. Rev. Lett. **100**, 136406 (2008).
[38] S. L. Dudarev, G. A. Botton, S. Y. Savrasov, C. J. Humphreys, and A. P. Sutton, Phys. Rev. B **57**, 1505 (1998).
[39] R. Sundararaman, P. Narang, A. S. Jermyn, W. A. Goddard III, and H. A. Atwater, Nat. Commun. **5**, 5788 (2014).
[40] I. Souza, N. Marzari, and D. Vanderbilt, Phys. Rev. B **65**, 035109 (2001).
[41] J. P. Perdew, K. Burke, and M. Ernzerhof, Phys. Rev. Lett. **77**, 3865 (1996).
[42] C. Voisin, N. Del Fatti, D. Christofilos, and F. Vallée, J. Phys. Chem. B **105**, 2264 (2001).
[43] J. H. Hodak, A. Henglein, and G. V. Hartland, J. Phys. Chem. B **104**, 9954 (2000).
[44] P. B. Allen, Phys. Rev. Lett. **59**, 1460 (1987).
[45] F. Giustino, M. L. Cohen, and S. G. Louie, Phys. Rev. B **76**, 165108 (2007).
[46] X. Y. Wang, D. M. Riffe, Y.-S. Lee, and M. C. Downer, Phys. Rev. B **50**, 8016 (1994).
[47] W. McMillan, Phys. Rev. **167**, 331 (1968).
[48] J. Hohlfeld, S.-S. Wellershoff, J. Güdde, U. Conrad, V. Jähnke, and E. Matthias, Chem. Phys. **251**, 237 (2000).
[49] C. Guo, G. Rodriguez, A. Lobad, and A. Taylor, Phys. Rev. Lett. **84**, 4493 (2000).
[50] B. Y. Mueller and B. Rethfeld, Phys. Rev. B **87**, 035139 (2013).
[51] F. Ladstädter, U. Hohenester, P. Puschnig, and C. Ambrosch-Draxl, Phys. Rev. B **70**, 235125 (2004).
[52] E. D. Palik, *Handbook of Optical Constants of Solids* (Academic Press, New York, 1985).
[53] A. D. Rakic, A. B. Djurišic, J. M. Elazar, and M. L. Majewski, Appl. Opt. **37**, 5271 (1998).
[54] See Supplemental Material at http://link.aps.org/supplemental/10.1103/PhysRevB.94.075120 for plots of the complex dielectric function at several electron temperatures, and complete data sets as a function of temperature and frequency for use in numerical analyses.
[55] R. Rosei, F. Antonangeli, and U. Grassano, Surf. Sci. **37**, 689 (1973).